

PRELIMINARY MISSION DETERMINATION FOR ASTEROID (29075) 1950DA

Evan A. Blosser *and Diogo Merguizo Sanchez[†]

This work focuses on the discovery of periodic orbits around the asteroid (29075) 1950DA. Utilizing Mass Concentration (MASCON) models of 1950DA, the 3-body problem is expanded to an N-body problem composed of the point cloud defining the models. This model is centered in the rotating, non-inertial, body-fixed frame. Equilibrium points were found using the algorithm for the Newton-Raphson method in 2-dimension, this was then furthered to 3-dimension. Quasi-periodic orbits were discovered from mesh grid simulations, and verified with a stability criteria of 60 days.

INTRODUCTION

The use of MASCON dates back to Muller and Sjogren, where the term was used for mass concentration near the Lunar surface.¹ Since then it has been used in numerous modeling techniques from the Earth and Moon to asteroids.² In essence, MASCON modeling is a method used to describe the irregularities in gravitational fields for non-uniform bodies, making it ideal for analyzing asteroids. The MASCON model consists of a particle cloud representing the center of mass (CM) of each tetrahedron that comprises the polyhedron shape model. The polyhedron shape models are created from radar imaging and light-curve inversion, and for our purposes, the polyhedron data is structured in Alias Waveform Format (OBJ). These OBJ shape model files can be found on multiple databases, but these in particular were taken from the NASA Jet Propulsion Lab (JPL) Asteroid Radar Research database.³

The target for this work is the asteroid (29075) 1950DA, which has been classified as a Near-Earth asteroid, and selected because of its close approach of only 0.05 AU to Earth in 2001. With an impact probability of 2.5×10^{-4} in 2880, 1950DA has been classified as a potentially hazardous asteroid (PHA).^{4,5} Solutions for shape models were generated for both a retrograde and prograde spin, with the understanding that the retrograde model was found to have no potential impact.⁶ For this reason, both models are used for both possibilities of rotational direction, with a spin period of 2.1216 ± 0.00004 hours.^{6,7} This is near the theoretical limit of ≈ 2.2 hr, thus 1950DA is a fast rotating rubble pile also classified as a strength-less asteroid.^{6,8} This classification comes from the fact that if 1950DA exceeds this rotational period limit, structural failure will occur as pieces of rubble begin to escape from the surface.⁹

*Graduate Research Assistant, Norman Astrodynamics Research Group. The University of Oklahoma, Norman, Oklahoma, 73019, AIAA Student Member

[†]Assistant Professor, School of Aerospace and Mechanical Engineering, The University of Oklahoma, 865 Asp Ave 73019 Norman OK, Member AAS/AIAA.

In this work, we examine XY, XZ, and YZ-frame slices of the asteroid's gravitational potential, and discover equilibrium points for the zero-velocity curves generated from the potential. Simulations over various initial distances and energies were conducted to show the nature of orbits surrounding the asteroid 1950DA. From this, we plot possible bounded orbits, along with trajectories that ended in collisions and escapes. Finally using a stability criteria of 60 days we verified a quasi-periodic orbit surrounding 1950DA.

MECHANICS OF MASCON

In order to understand this method we look no further than *The Theory of the Potential* which dictates the manner in which gravitational potentials are calculated for MASCON models. By Newton's Law of gravitational attraction for a grouping of particles, we see the attraction of the m_0 particle being the force vector summation of the masses m_i for $i = 1, 2, \dots, N$.¹⁰ Here, and throughout this work, N will be defined as the number of tetrahedron CMs within the MASCON model. Figure 1 depicts the force vectors of each m_i particle on the singular m_0 particle. For the case of MASCON, we treat the m_0 particle as the external orbiting particle and define the m_i particles as the MASCON model.

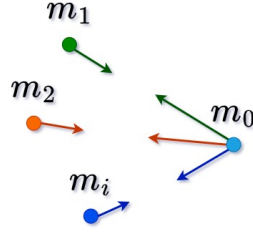


Figure 1. Depiction of force vectors for a particle cloud of size m_i acting on a single particle m_0 .

We note that this definition of vector summation only holds true for particles and not bodies of finite sizes. To this end, we subject the asteroid model to a decomposition of the finite body and imagine a cloud of mass concentrated within a given space. Thus, the designation MASCON signifies the assumption made regarding the asteroid's structure.

The mathematical coupling of the particle m_0 with each particle m_i can be seen below in Eq. (1) and further in Eq. (2) through (10). Here we define each m_i particle coordinate by ξ_i, η_i, ζ_i with respect to our Cartesian coordinate system. The particle m_0 takes the x, y, z coordinates, and remains constant through the summation of the force vectors for each position in space.

$$r_i = \sqrt{(\xi_i - x)^2 + (\eta_i - y)^2 + (\zeta_i - z)^2} \quad (1)$$

We see this coupling further when we examine the direction cosines of the lines of force, as follows:

$$\frac{\xi_i - x}{r_i}, \quad \frac{\eta_i - y}{r_i}, \quad \frac{\zeta_i - z}{r_i}. \quad (2)$$

These equations reflect the direction of each gravitational force vector of the particles m_i acting upon m_0 within our given space. These direction cosines are also reflected within Eq. (4) through

Eq. (9). These reflections show the influence each particle within the m_i mass concentration has upon the external orbiting particle m_0 .

With this we are able to define the gravitational potential of a particle cloud acting upon an orbiting external particle with mass m_0 in Eq. (3). Here we note that μ_i defines the gravitational parameter for each individual tetrahedron as, $\mu_i = Gm_i$, with Newton's gravitational constant taken to be approximately 6.67430×10^{-20} km³/kgs².

$$U = \sum_{i=1}^N \frac{\mu_i}{r_i} \quad (3)$$

Following this equation, are the gradients of the potential in Cartesian coordinates.

$$U_\xi = - \sum_{i=1}^N \frac{\mu_i(x - \xi_i)}{r_i^3} \quad (4)$$

$$U_\eta = - \sum_{i=1}^N \frac{\mu_i(x - \eta_i)}{r_i^3} \quad (5)$$

$$U_\zeta = - \sum_{i=1}^N \frac{\mu_i(x - \zeta_i)}{r_i^3} \quad (6)$$

The hessian of the gravitational potential is as follows.¹¹

$$U_{\xi\xi} = - \sum_{i=1}^N \left(-\frac{\mu_i}{r_i^3} + \frac{3\mu_i(x - \xi_i)^2}{r_i^5} \right) \quad (7)$$

$$U_{\eta\eta} = - \sum_{i=1}^N \left(-\frac{\mu_i}{r_i^3} + \frac{3\mu_i(y - \eta_i)^2}{r_i^5} \right) \quad (8)$$

$$U_{\zeta\zeta} = - \sum_{i=1}^N \left(-\frac{\mu_i}{r_i^3} + \frac{3\mu_i(z - \zeta_i)^2}{r_i^5} \right) \quad (9)$$

$$U_{\xi\eta} = - \sum_{i=1}^N \left(\frac{3\mu_i(x - \xi_i)(y - \eta_i)}{r_i^5} \right) \quad (10)$$

where for remaining hessian components are found with Eq. (10) & defining $\xi \neq \eta \neq \zeta$

THE MASCON MODEL AND PHYSICAL PROPERTIES OF 1950DA

The MASCON model is comprised of the tetrahedron CMs. These CMs can be found by using a weighted average between the face vertices of each tetrahedron and the polyhedron CM. This creates the cloud of points that define each tetrahedron's CM within the face mesh as seen in Figure 2. The polyhedron CM was calculated using the software `volInt.c` or "Volume Integration". This software was created by Brian Mirtich in 1996 and has been widely used to calculate the: volume,

Volume		
	Prograde Model	Retrograde Model
Busch <i>et al.</i> (2007)	$0.82 \text{ km}^3 (\pm 30\%)$	$1.14 \text{ km}^3 (\pm 30\%)$
volInt.C	$\approx 0.15328 \text{ km}^3$	$\approx 1.15329 \text{ km}^3$
analytical	$\approx 0.90525 \text{ km}^3$	$\approx 0.96665 \text{ km}^3$
Numpy	$\approx 0.73623 \text{ km}^3$	$\approx 1.08646 \text{ km}^3$
γ	0.99034	1.00973

Table 1. Volume Calculations for 1950DA.

moments, and products of inertia, as well as the CM of polyhedron shape models for asteroids in numerous works.¹² Each model’s OBJ was passed through the software to produce the polyhedron CM used alongside the OBJ to create the shape model shown in Figure 2.

Within previous works of Busch *et al.*, the volume for 1950DA has been calculated with a $\pm 30\%$ error for both models. With this they also calculated the densities for both models; they found the prograde model has a minimum strength-less bulk density of $3.0 \text{ g cm}^{-3} \pm 10\%$, and the retrograde has a density of $3.5 \text{ g cm}^{-3} \pm 10\%$.⁶ This was furthered when a minimum Bulk density with respect to the cohesive strength of 1950DA was examined and found to be $1.7 \pm 0.7 \text{ g cm}^{-3}$.⁹ Thus, this density was used within this work’s calculations, yet the volumes were re-calculated for this work using both `volInt.c` and analytically within Python.

The analytical methods used for this work utilized the triple scalar product for each individual tetrahedron within the polyhedron shape. This calculation is shown in Eq. (11) takes each vector X, Y, Z drawn by the vertices of the tetrahedron and polyhedron CM, and calculates the volume. The tetrahedron calculations are then summed to calculate the total volume of the shape model.

$$V = \frac{1}{6}(u \times v \cdot w) = \frac{1}{6} \begin{vmatrix} X_1 & Y_1 & Z_1 \\ X_2 & Y_2 & Z_2 \\ X_3 & Y_3 & Z_3 \end{vmatrix} \quad (11)$$

Equation (11) was coded into Python and calculated analytically, however, Numpy’s `dot()` and `cross()` functions were also used to ensure calculations were accurate.¹³ These calculations presented in Table 1 show a varying degree of accuracy, thus a ratio was created between the value calculated by Busch *et al.* and this work’s calculations. For the prograde model calculations the analytical calculation of 0.90525 km^3 was accepted, and the value calculated by Numpy was accepted for the retrograde model.

It should be noted, that by physical examination of the shape, the prograde model is far more concave, which for the algorithm of Mirtich used in `volInt.c` can yield inconsistencies with volumetric calculations. However, the overall usefulness of its fast calculations of moments and products of inertia should not be diminished.

These calculations utilized the diameter of the equal-volume sphere, presented by Busch *et al.* along with the shape models for the prograde and retrograde spins.⁶ The prograde had a diameter of $1.16 \text{ km} \pm 10\%$ and the retrogrades diameter was $1.30 \text{ km} \pm 10\%$.⁶ From this, the effective radius R_{eff} was calculated and used for the scaling factor γ , and producing the models shown in Fig. 2:

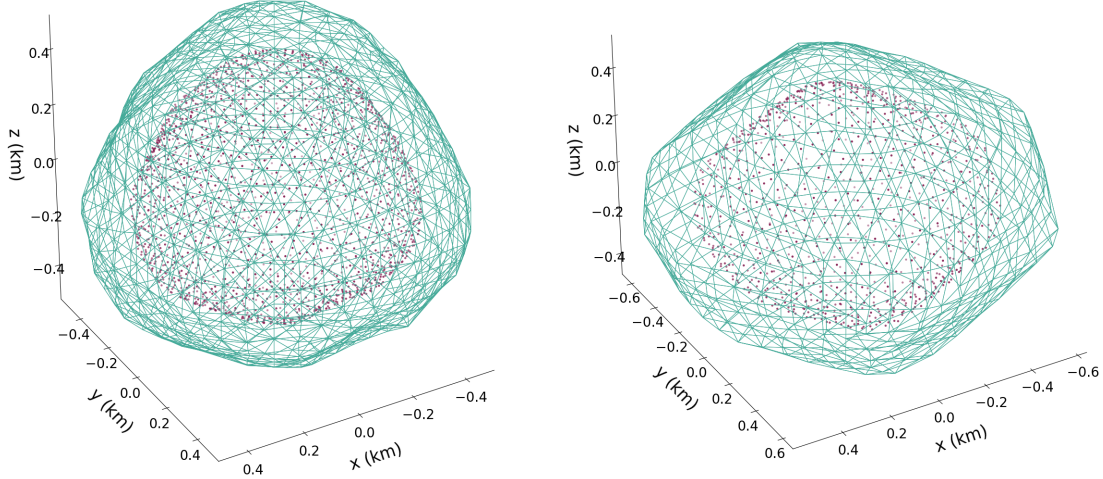


Figure 2. Models of 1950DA represented in MASCON I. Left: Prograde model with a total of 2036 CMs, and $R_{eff} = 0.58$ km. Right: Retrograde model with a total of 1016 CMs, and $R_{eff} = 0.65$ km.

Mass kg	
Prograde Model	Retrograde Model
$1.538918 \times 10^{12} \pm 0.7$ kg	$1.846980 \times 10^{12} \pm 0.7$ kg

Table 2. Mass calculations for 1950DA, using this works volume calculations and the minimum bulk density of 1.7 ± 0.7 g cm $^{-3}$.

From the volume, several mass calculations have been conducted on 1950DA, within the cohesive strength study conducted by Rozitis *et al.*, the asteroid had $2.1 \times 10^{12} \pm 1.1$ kg, showing the uncertainty for the physical properties of 1950DA.⁹ Because of this uncertainty, we calculated the mass using the more recent density for the asteroid, 1.7 ± 0.7 g cm $^{-3}$, which carries less uncertainty with it when calculating the mass of the asteroid as $m = \rho V$.

Table 2 shows the mass calculations for this work, which was used within the simulated orbits shown later in Figure 8 through 11. We can see that these calculations carry with them less uncertainty, however, there is still an unknown amount of uncertainty within the volume. Defined within Table 1, the volume calculations carry a $\pm 30\%$ uncertainty to them, and we can assume that our calculations also carry this uncertainty.

GRAVITATIONAL POTENTIAL OF 1950DA

To define the potential of the asteroid we use the following Hamiltonian equation of motion:

$$H = \underbrace{\frac{1}{2}(\dot{x}^2 + \dot{y}^2 + \dot{z}^2)}_{Kinetic\ Energy} - \underbrace{\frac{1}{2}\omega^2(x^2 + y^2)}_{Potential\ Energy} - U \quad (12)$$

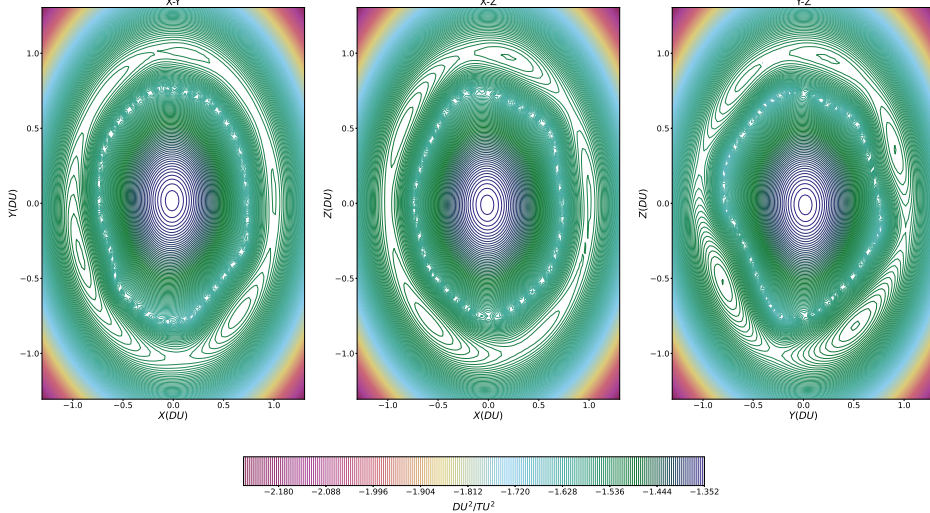


Figure 3. Equipotential plots of the prograde model in non-dimensional units.

Where U is defined by Eq. 3, we then set the kinetic energy to zero, thus giving us the potential energy for the zero-velocity curve:

$$\text{Potential Energy} = -\frac{1}{2}\omega^2(x^2 + y^2) - U \quad (13)$$

Within Eq. 13 we see the terms for the Coriolis force are left along with the potential for the asteroid. Given the fast rotation of 1950DA, we can see that the Coriolis force can be the dominating term. This is furthered when we look at the uncertainty of mass and volume calculations, thus the potential is defined in a non-dimensional system where we set the *Distance Unit DU* to be the effective radius of the asteroid 1 DU = R_{eff} (km). Figure 3 and 4 show these potentials in slices of XY, XZ, and YZ-frame where the non-dimensionalizing leads to $\omega = 1$ thus reducing it from Eq. (13), and allowing for a detailed analysis of the potential near the asteroid in the body-fixed rotating frame. These figures define several possible stable equilibrium points, that could then lead to the plotting of stable orbits. There is also several separatrixs that define saddle point position. These saddle points serve as unstable equilibrium positions and would require additional propellant consumption in order to maintain a stable orbit.

EQUILIBRIUM POINTS FOR AN ORBITING PARTICLE

A 2-dimensional Newton-Raphson method was used to find the equilibrium points in the XY-frame following the algorithm depicted by Daniel Scheeres.¹⁴ First, we define an incremental change δx_i to the initial guess x_i . If this approximately satisfies $H_x(x_i + \delta x_i) = 0$, then we can use a Taylor series in the first order to expand the function and solve for this incremental change:

$$H_x(x_i) + H_{xx}(x_i) \cdot \delta x_i + \dots = 0 \quad (14)$$

The solution update is found as follows:

$$\delta x_i = -H_{xx}(x_i)^{-1} \cdot H_x(x_i) \quad (15)$$

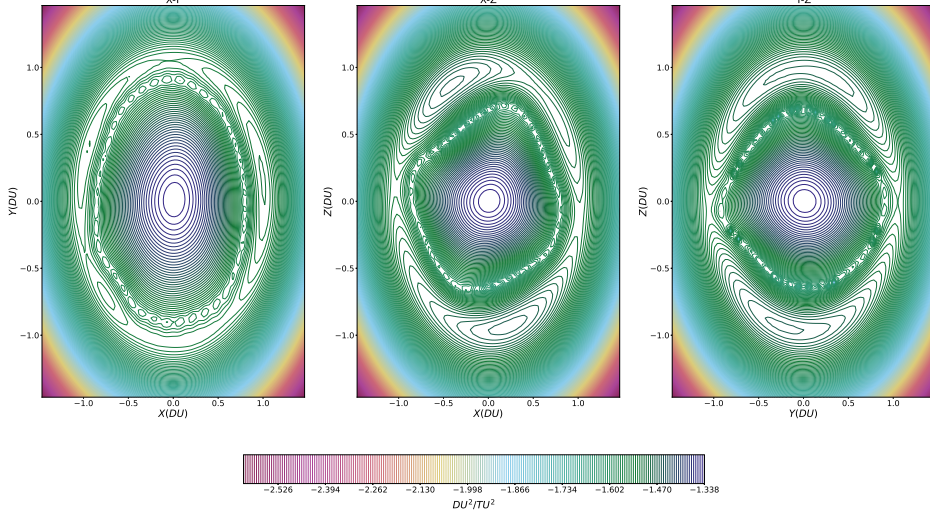


Figure 4. Equipotential plots of the retrograde model in non-dimensional units.

$$x_{i+1} = x_i + \delta x_i \quad (16)$$

Using this algorithm, we define the system as the Hamiltonian equation of motion, where we set $\dot{x} = \dot{y} = 0$, yielding the following equations:

$$0 = \omega^2 x + U_\xi \quad (17)$$

$$0 = \omega^2 y + U_\eta \quad (18)$$

Where we see that Eq. (4)and (5) are present within the gradient of the potential, as the gradient of the asteroid's potential, along with the partial derivatives of the Coriolis force. Equations (17) and (18) are set into the algorithm's form as:

$$H_x = \begin{bmatrix} \omega^2 x + U_\xi \\ \omega^2 y + U_\eta \end{bmatrix} \quad (19)$$

For our given non-denationalization, we set $\omega = 1$, yielding the reduced form:

$$H_x = \begin{bmatrix} x + U_\xi \\ y + U_\eta \end{bmatrix} \quad (20)$$

Subsequently using Eq. (7) through(10), the derived hessian of the asteroid's gravitational potential, we define the H_{xx} matrix within the algorithm as follows:

$$H_{xx} = \begin{bmatrix} U_{\xi\xi} & U_{\xi\eta} \\ U_{\eta\xi} & U_{\eta\eta} \end{bmatrix} \quad (21)$$

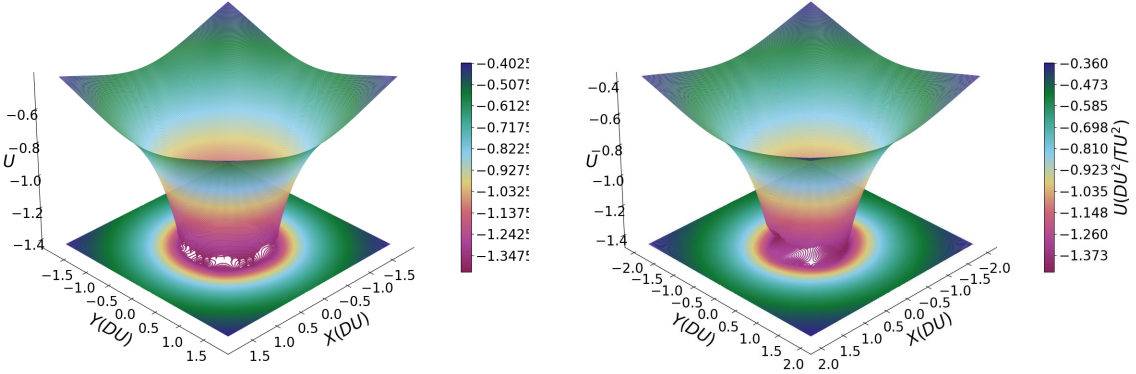


Figure 5. XY-slices of 1950DA Left: Prograde model. Right: Retrograde model.

Prograde Model Equilibrium Points		
	x (DU)	y (DU)
E_1	-0.923045	-0.347635
E_2	-0.011768	0.017731
E_3	0.147349	0.999011
E_4	-0.657543	-0.735743
E_5	0.999436	0.081049

Table 3. Equilibrium positions calculated within approximately 26.4 seconds using Newton-Raphson's method in 2-dimensions.

Thus, we find each update to finding the solution as follows:

$$\delta x_i = -H_{xx}^{-1} \cdot H_x = -\begin{bmatrix} U_{\xi\xi} & U_{\xi\eta} \\ U_{\eta\xi} & U_{\eta\eta} \end{bmatrix}^{-1} \cdot \begin{bmatrix} x + U_\xi \\ y + U_\eta \end{bmatrix} \quad (22)$$

This algorithm was then coded into Python, and produced the equilibrium points presented within Table 3 and shown in the X-Y frame in Figure 6. We see both in the table and figure, that E_2 is a central equilibrium and serves as a check to the program. This comes from the understanding that the center of the asteroid is the true equilibrium, yet is redundant for future missions as it lies in the center of the asteroid and is inaccessible.

The Newton-Raphson method in 2-dimensions was then expanded to 3-dimensions as follows:

$$\delta x_i = -\begin{bmatrix} U_{\xi\xi} & U_{\xi\eta} & U_{\xi\zeta} \\ U_{\eta\xi} & U_{\eta\eta} & U_{\eta\zeta} \\ U_{\zeta\xi} & U_{\zeta\eta} & U_{\zeta\zeta} \end{bmatrix}^{-1} \cdot \begin{bmatrix} x + U_\xi \\ y + U_\eta \\ z + U_\zeta \end{bmatrix} \quad (23)$$

Utilizing similar methods equilibrium points were found in the 3D Cartesian coordinate frame. Table 4 shows the solutions for the equilibrium position of the prograde model. Some of these were found to lay within the body and are thus merely checks to the validity of the program, as gravitational equilibrium should exist inside the body. These points near the surface can be utilized as possible landing positions for the asteroid.

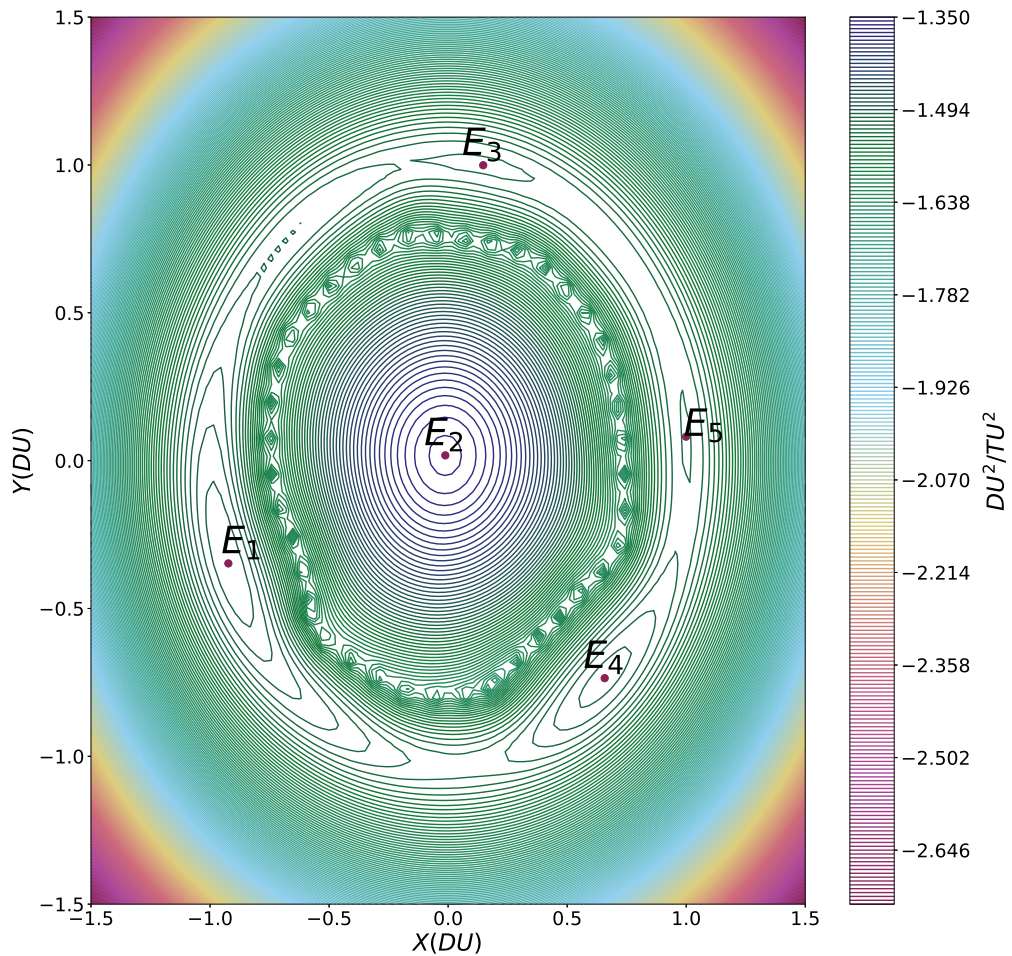


Figure 6. Equilibrium points found using the Newton-Raphson method in 2D for the XY-frame.

Prograde Model Equilibrium Points			
	x (DU)	y (DU)	z (DU)
E_1	0.80429	0.60987	0.03082
E_2	-0.17279	1.01053	-0.05477
E_3	0.27216	-0.30391	1.603328
E_4	0.05916	-1.03755	0.06762
E_5	0.50059	0.00525	-0.52285

Table 4. Equilibrium positions calculated within approximately 38 minutes and 50.5 seconds using Newton-Raphson's method in 3 dimensions.

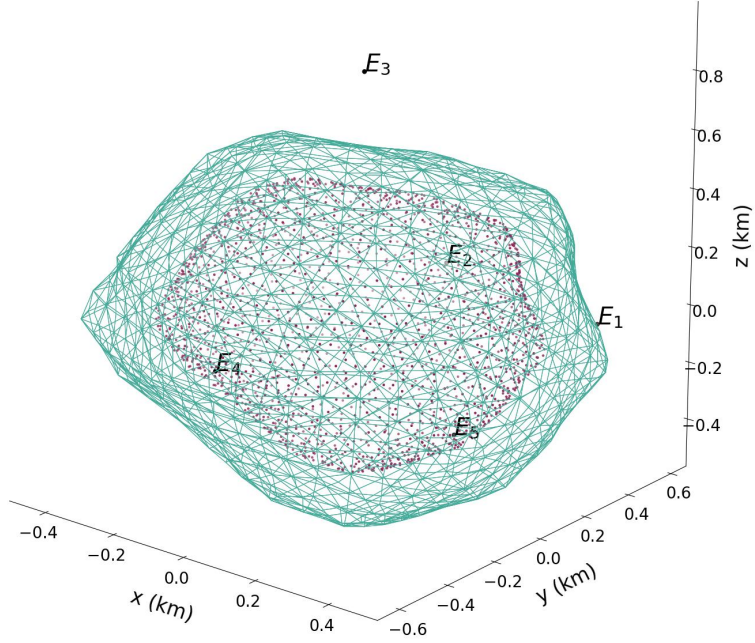


Figure 7. Equilibrium point E_3 , in 3-dimensions shown near the prograde model.

The Equilibrium point E_3 in particular, when converted back into dimensional units using the effective radius is:

$$E_3(0.15785, -0.17627, 0.92993) \text{ km}$$

The point E_3 is shown as an external equilibrium position within Figure 7. It should be noted here that simulations were not conducted to check the validity of the equilibrium points. These are approximate equilibrium points found in a non-dimensional system, which may lead to a stable equilibrium point with more investigation.

STABLE TRAJECTORIES

We utilized Eq. (25) through (27) in the body-fixed rotating frame. Thus we imagine our MASCON model as a particle cloud of size N rotating about the center, defined as the polyhedron's

center of mass. This is shown in Eq. 24, where \vec{R} takes the place of ξ_i, η_i, ζ_i within Eq 1. These equations were coded into Python to produce the simulation results shown in Figure 8.

$$\vec{R} = \vec{r}_{tetra} - \vec{r}_{poly} \quad (24)$$

$$\ddot{x} = \omega^2 x + 2\omega\dot{y} + U_\xi \quad (25)$$

$$\ddot{y} = \omega^2 y - 2\omega\dot{x} + U_\eta \quad (26)$$

$$\ddot{z} = U_\zeta \quad (27)$$

For the simulation, we set $x = z = \dot{y} = \dot{z} = 0$, and use y as our position solving for \dot{x} as our velocity. By doing so we set our simulation in a hyperplane, using the initial conditions as the starting point, yet we allow this to develop into the z-axis as Eq. 27 is not set to zero. This can be seen in Figures 9 through 11 were the perturbations from the asteroid draws the orbit down from the hyperplane. For the bounded orbit we can see the ascension back to the hyperplane. We can see the cross-hair pattern that defines this motion in Figure 9.

For the initial conditions of the simulation, we looked at energies ranging from $H = 1 \times 10^{-6} \text{ km}^2/\text{s}^2$ to $H = 1 \times 10^{-5} \text{ km}^2/\text{s}^2$, and a distance of 1 to 10 km. The step sizes between each simulation was $0.25 \times 10^{-7} \text{ km}^2/\text{s}^2$ and 0.25 km. For collision detection, the limit of the body was taken to be the effective radius of the asteroid which is 0.58 km for the prograde model.

The orbital simulations conducted within this work utilized the SciPy integrator `solve_ivp()` for its explicit Runge-Kutta method of order 8.¹⁵ The total simulation time for Figure 8 was 1 day and served as a preliminary stability criterion for bounded orbits. The stability criteria of 60 days was selected to verify the bounded orbits. This stability criterion comes with the assumption of no additional perturbations. This verification can be seen within Figure 9 where the total 60-day simulation was completed without collision or escape.

The sphere of influence of the asteroid was calculated for the purpose of understanding the influence of the Sun on distant orbits, and that of the escape trajectories.¹⁶ The sphere of influence will be used as a boundary for simulation to show when an orbiting particle will leave the influence of 1950DA and not return. Equation 28 shows the calculation made for the asteroid using the semi-major axis of 1950DA's orbit as an average between the periapsis and apoapsis, as each position will lead to varying results.

$$R_H = R \left(\frac{m_{body}}{M_\odot} \right) \quad (28)$$

The semi-major axis value for 1950DA's orbit was taken from JPL Horizons, and using the mass of the sun as approximately 132712440018 kg, the sphere of influence was calculated to be ≈ 14.46513 km. In order to set a definite escape limit for the simulated orbits, the calculation for the sphere of influence was multiplied by 5, yielding 72.32565 km. This ensured that any escaped orbit was a true escape with no return.

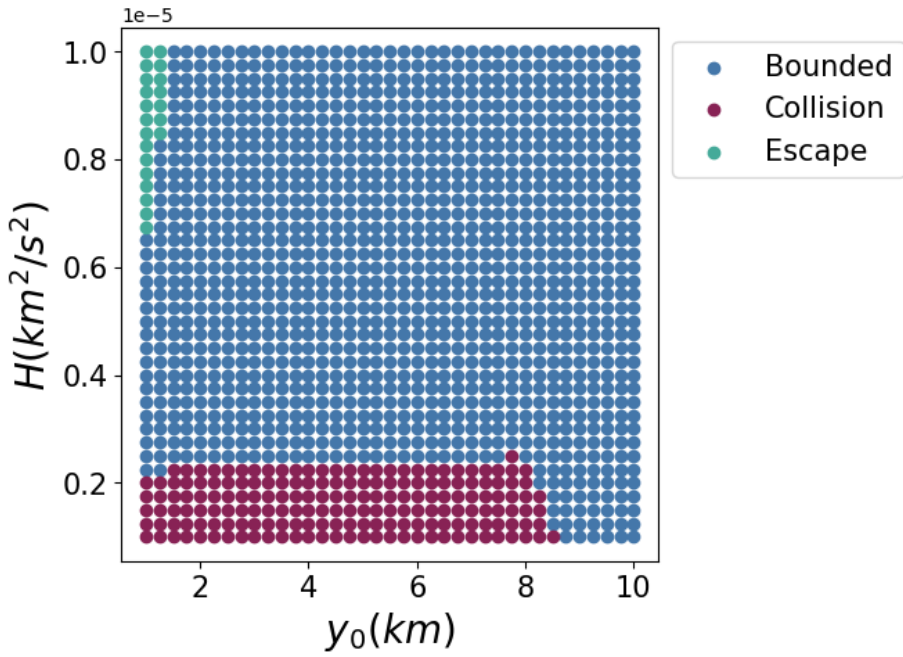


Figure 8. Simulated orbits around the Prograde model of 1950DA, for 1 day total, with a step size of $\Delta t = 1.0$ sec, the simulation completed within: 55.052 hours.

Mesh Grid Size	Regular (Sec)	TensorFlow (Sec)	Multiprocessing (Sec)
100	0.08314 ± 0.00232 .	1.35401 ± 0.14727	8.73846 ± 0.26053
1,000	33.48606 ± 1.56878	8.93515 ± 0.54915	22.08205 ± 1.02119
10,000	3627.16058 ± 293.50415	823.66046 ± 55.70785	2219.72157 ± 31.04704

Table 5. Times for the processing speed experiment.

One of the bounded orbits, shown in Figure 9, meets the preliminary and verification stability criteria of 1 and 60 days respectively. We see that it varies by roughly 20 m in the z-axis, yet holds as a quasi-periodic orbit with respect to the XY-frame. The other orbits shown in Figure 10 and 11 are of a collision and escape trajectory respectively. These were taken from the simulation conducted which also produced the results shown in Figure 8. The quasi-periodic orbit can be seen in perspective with the asteroid in Figure 12, showing the development in the z-axis minimal.

DECREASING PROCESSING SPEED

Using the Python modules TensorFlow and the built-in Multiprocessing, experiments were performed on the equipotential plots.¹⁷ 3 processes were made, one was designated as regular and used basic calculation techniques with NumPy in Python. In order to fully utilize the capabilities TensorFlow has with the Graphics Processing Unit (GPU), several specific programs had to be installed mainly the actual **tensorflow-gpu**, as the regular distribution will only utilize the Central Processing Unit (CPU). The specific distribution we used was **tensorflow-gpu** 2.10.1, along with **tensorflow** 2.17, yet for this to work properly additional software had to be installed. Compute Unified Device Architecture (CUDA) 11 and the supporting CUDA Deep Neural Network library (cuDNN) 8.9.7

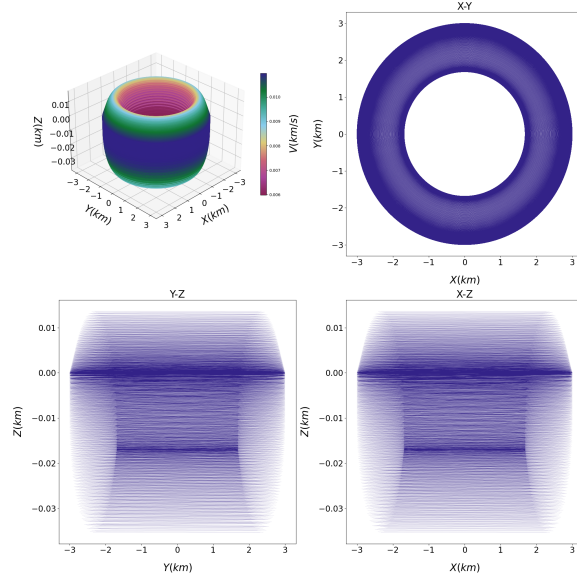


Figure 9. Bounded orbit simulated around 1950DA prograde model, for 60 days, with a $\Delta t = 50$ sec with the initial position of $y_0 = 3.0$ km and an energy of $H = 3.0 \times 10^{-6} \text{ km}^2/\text{s}^2$.

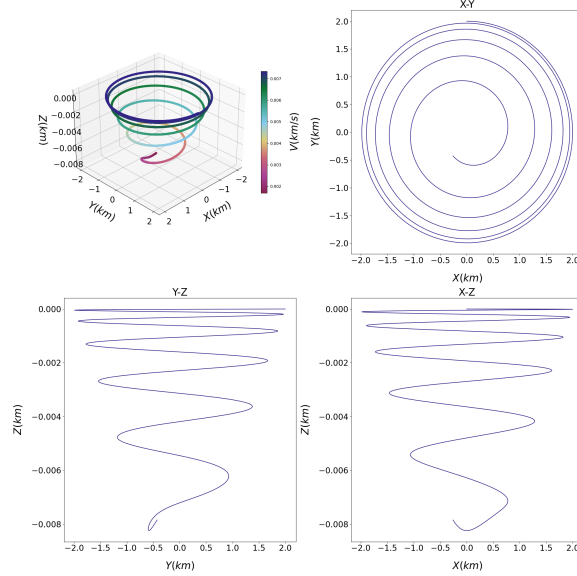


Figure 10. Simulated orbit around the 1950DA prograde model that ended in a collision after approximately 2.685 hours. The initial conditions for this collision were $y_0 = 2.0$ km and $H = 1 \times 10^{-6} \text{ km}^2/\text{s}^2$.

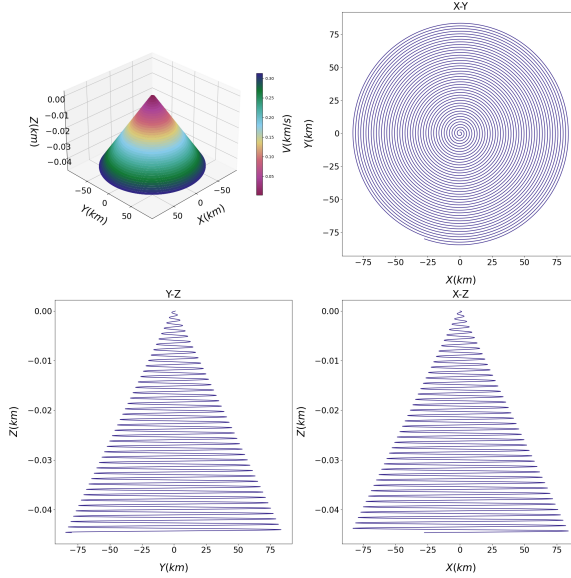


Figure 11. Simulated orbit around the 1950DA prograde model that ended in an escape after approximately 19.708 hours. The initial conditions for this escape were $y_0 = 1.0 \text{ km}$ and $H = 8 \times 10^{-6} \text{ km}^2/\text{s}^2$.

was installed in order for **tensorflow-gpu** to access the GPU for calculations.

For the task to be performed, each process would complete a calculation for the zero-velocity curves similar to the ones presented within Figure 3 and 4. Three selected sizes of the meshgrid: 100, 1,000, and 10,000 were used to analyze the calculation speed of each process. These processes were carried out a total of 50 times for the first two sizes, however for the 10,000 size mesh grid only 5 total runs were conducted to minimize any possible damage to the CPU. This test, along with the rest of the simulations, was performed using an Intel i9-9900K@3.60 Hz CPU, and an Nvidia GeForce RTX-3060 GPU.

The experiment results can be seen in Table 5, and show that while the size of calculations remains relatively low, the regular Python method is more than sufficiently fast as compared to the other two methods. However, for increased sizes of the mesh grid, both Multiprocessing and TensorFlow outperformed the regular calculations. As seen in Table 5 the TensorFlow process completed in roughly 13.73 minutes for the mesh grid of 10,000, while the regular calculations took over an hour with roughly 60.45 minutes of calculation time. It should be noted that even though the Multiprocessing was indeed faster than the regular process once the mesh grid increased, to achieve this result all cores of the CPU had to be utilized. Reinforcing the decision to limit the mesh grid size of 10,000 to only 5 runs.

This is due to the capabilities of the GPU for Tensor calculation. There is a significant error when dealing with TensorFlow as it uses $\text{float} = 32$ as its data type, while Numpy uses $\text{float} = 64$. This means that Tensorflow loses accuracy as can be seen in Figure 13. Overall there is a $\pm 0.8\%$ error when using TensorFlow as compared to regular Python calculations.

There are additional limitations when using TensorFlow, as it is not compatible with Python integrators such as `solve_ivp()`. Thus, the use of it to speed up simulations yielded no results. Multiprocessing in this regard is also hard to implement as it requires creating chunks of each

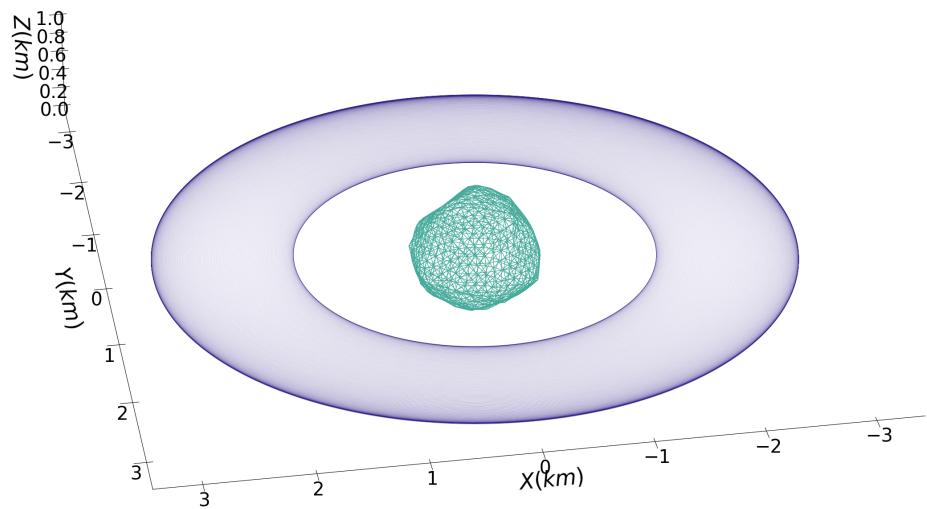


Figure 12. Bounded orbit simulated around 1950DA prograde model, for 60 days, with the initial position of $y_0 = 3.0$ km and an energy of $H = 3.0 \times 10^{-6} \text{ km}^2/\text{s}^{-2}$. Shown with the asteroids **OBJ** for scale.

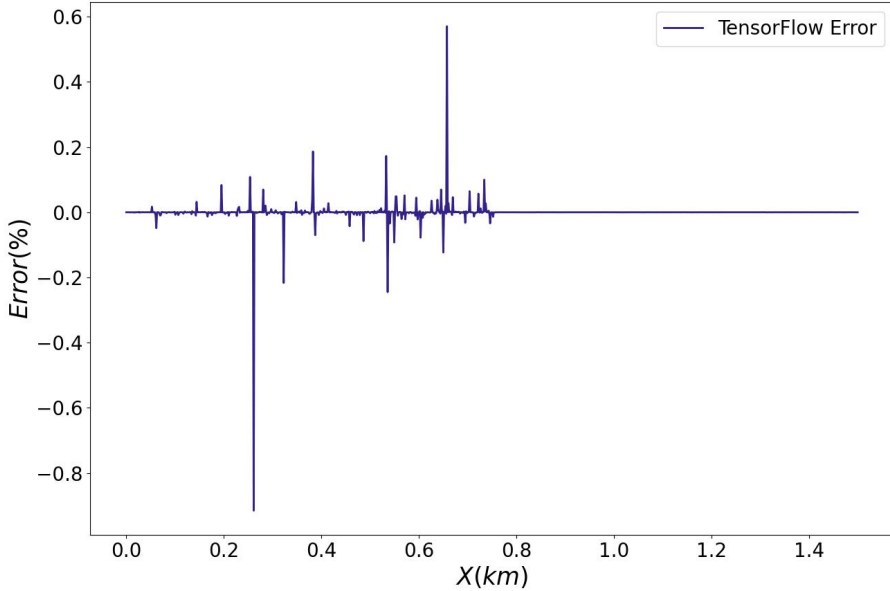


Figure 13. Error for Regular Vs. TensorFlow methods, calculate the gravity potential for a particle moving in the x-direction; for this, we set $y=z=0$.

part of the mesh grid to send to each CPU core for calculations, making it unable to be used with integrators. However, with all this said it is clear that increasing the size of calculations leads to an exponential increase in calculation times, and by using TensorFlow or Multiprocessing you can greatly mitigate the exponential increase's rate allowing for larger calculations.

CONCLUSION

From the simulations, we can see that energies of approximately $H \leq 2.5 \times 10^{-6} \text{ km}^2/\text{s}^2$ and under 8.5 km in distance will lead to a collision with the asteroid. In contrast the initial conditions of $y_0 \leq 1.25 \text{ km}$ with higher energies $H \geq 6.75 \times 10^{-6} \text{ km}^2/\text{s}^2$ lead to an escape trajectory. The region inside these conditions, however, led to possible bounded orbits. A bounded quasi-periodic was then verified for the position $y_0 = 3.0 \text{ km}$ with an energy of $H = 4 \times 10^{-6} \text{ km}^2/\text{s}^2$ with a stability criteria of 60 days. Equilibrium points were found within a non-dimensional system using the Newton-Raphson method in 2 and 3- dimensions. An external point was found at approximately $E_3(0.15785, -0.17627, 0.92993) \text{ km}$. However, this point's equilibrium has not been verified in simulation.

The results from the processing time experiment yielded a surprisingly fast time for TensorFlow as compared to the other two processes. With a calculation time of only 13.73 minutes as compared to over an hour of processing time for regular Python, the use of TensorFlow can be seen as ideal for decreasing processing times. For the promise of future missions, the code in this work was built to be able to be utilized and optimized for minimal run times. However, as shown optimization may not be possible with TensorFlow or Multiprocessing for any lengthy orbital simulations for future missions. This code can also be universally implemented with the asteroids that we have shape

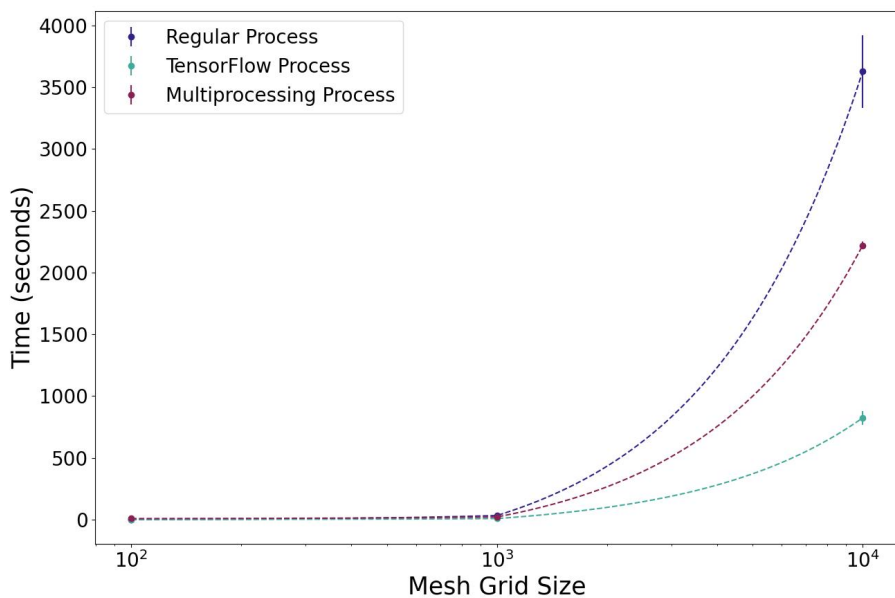


Figure 14. Interpolated values detailing exponential curves of calculation times for the processing time experiment.

models for, given that we have some assumptions about the asteroid's properties.

ACKNOWLEDGMENT

I would like to thank my advisor Dr. Diogo Merguizo Sanchez for teaching and guiding me along on my path of research in the world of astrodynamics, and I would like to thank my family for all of the love and support!

⌚ Git-hub's Co-pilot aided in the learning process and coding of this software.

NOTATION

V volume
 ρ density

The `volInt.c` software can be found at:

➔ [graphspenFOAM-2.1.x](#)[accessed April 10.2024]

Newton's Gravitational Constant was found at:

➔ <https://physics.nist.gov/cgi-bin/cuu/Value?bg>

Dr. Paul Tol, a Dutch instrument scientist with a PhD. in atomic physics, created the color-blind friendly palette used for all graphs. The explanation of the palette creation can be found here:

➔ <https://personal.sron.nl/~pault/>

The palette can be found along with many more on Dr. David Nichols' online Coloring for Colorblindness tool:

➔ <https://davidmathlogic.com/colorblind/>

The code for the processing time experiment can be found in the following GitHub repository:

⌚ https://github.com/evan-a-blosser-1/1950DA_Preliminary_Mission

REFERENCES

- [1] P. M. Muller and W. L. Sjogren, "Mascons: Lunar Mass Concentrations," *Science*, Vol. 161, Aug. 1968, pp. 680–684, 10.1126/science.161.3842.680.
- [2] M. Antoni, "A review of different mascon approaches for regional gravity field modelling since 1968," *History of Geo- and Space Sciences*, Vol. 13, Sept. 2022, pp. 205–217, 10.5194/hgss-13-205-2022.
- [3] L. A. Benner, "Asteroid radar research,"
- [4] J. D. Giorgini, S. J. Ostro, L. A. M. Benner, P. W. Chodas, S. R. Chesley, R. S. Hudson, M. C. Nolan, A. R. Klemola, E. M. Standish, R. F. Jurgens, R. Rose, A. B. Chamberlin, D. K. Yeomans, and J.-L. Margot, "Asteroid 1950 DA's Encounter with Earth in 2880: Physical Limits of Collision Probability Prediction," *Science*, Vol. 296, Apr. 2002, pp. 132–136, 10.1126/science.1068191.
- [5] D. Farnocchia and S. Chesley, "Assessment of the 2880 impact threat from Asteroid (29075) 1950 DA," *Icarus*, Vol. 229, Feb. 2014, pp. 321–327, 10.1016/j.icarus.2013.09.022.

- [6] M. BUSCH, J. GIORGINI, S. OSTRO, L. BENNER, R. JURGENS, R. ROSE, M. HICKS, P. PRAVEC, P. KUSNIRAK, and M. IRELAND, “Physical modeling of near-Earth Asteroid (29075) 1950 DA,” *Icarus*, Vol. 190, Oct. 2007, pp. 608–621, 10.1016/j.icarus.2007.03.032.
- [7] M. Hirabayashi and D. J. Scheeres, “STRESS AND FAILURE ANALYSIS OF RAPIDLY ROTATING ASTEROID (29075) 1950 DA,” *The Astrophysical Journal*, Vol. 798, Dec. 2014, p. L8, 10.1088/2041-8205/798/1/8.
- [8] P. Pravec and A. W. Harris, “Fast and Slow Rotation of Asteroids,” *Icarus*, Vol. 148, Nov. 2000, pp. 12–20, 10.1006/icar.2000.6482.
- [9] B. Rozitis, E. MacLennan, and J. P. Emery, “Cohesive forces prevent the rotational breakup of rubble-pile asteroid (29075) 1950 DA,” *Nature*, Vol. 512, Aug. 2014, pp. 174–176, 10.1038/nature13632.
- [10] W. D. MacMillan, *The Theory of the Potential*. Dover Publications, Inc., 1958.
- [11] S. Aljbaae, T. G. G. Chanut, V. Carruba, J. Souchay, A. F. B. A. Prado, and A. Amarante, “The dynamical environment of asteroid 21 Lutetia according to different internal models,” *Monthly Notices of the Royal Astronomical Society*, Vol. 464, Oct. 2016, pp. 3552–3560, 10.1093/mnras/stw2619.
- [12] B. Mirtich, “Fast and Accurate Computation of Polyhedral Mass Properties,” *Journal of Graphics Tools*, Vol. 1, Jan. 1996, pp. 31–50, 10.1080/10867651.1996.10487458.
- [13] “NumPy documentation - NumPy v2.0 Manual.”
- [14] D. J. Scheeres, *Orbital Motion in Strongly Perturbed Environments*. SpringerLink, Berlin, Heidelberg: Springer Berlin Heidelberg, 2012.
- [15] “SciPy documentation.”
- [16] H. Curtis, *Orbital Mechanics for Engineering Students Revised Reprint*. Elsevier Science Technology, 2020.
- [17] “TensorFlow v2.16.1,”